Electronic Supplementary Material (ESI) for Journal of Materials Chemistry A.
This journal is © The Royal Society of Chemistry 2022

$Ge_{1-x}Mn_xTe$ Electronic Supplementary Information

Jesse M. Adamczyk,[†,¶] Ferdaushi A. Bipasha,[‡,¶] Grace A. Rome,[†] Kamil Ciesielski,[†] Elif Ertekin,[‡] and Eric S. Toberer[*,†]

†*Department of Physics, Colorado School of Mines, Golden, CO, USA*

‡*Department of Mechanical Science and Engineering, University of Illinois Urbana Champaign, Urbana, IL 61801, USA*

¶*First authorship is shared as a result of equal intellectual contributions.*

E-mail: etoberer@mines.edu

Table 1: Table of carrier concentration values for samples shown in main text.

Sample Composition	Carrier Concentration (cm-3)
Mn0.05Ge0.47Te0.48	9.1E20
Mn0.105Ge0.39Te0.505	2.4E20
Mn0.14Ge0.38Te0.45	1.3E20
Mn0.16Ge0.3Te0.54	2.8E20
Mn0.2Ge0.325Te0.475	1.5E20
Mn0.2Ge0.225Te0.575	1.8E20
Mn0.25Ge0.25Te0.5	1.5E20
Mn0.29Ge0.25Te0.45	1.4E20
Mn0.32Ge0.21Te0.47	2.0E20
Mn0.325Ge0.175Te0.5	1.2E20

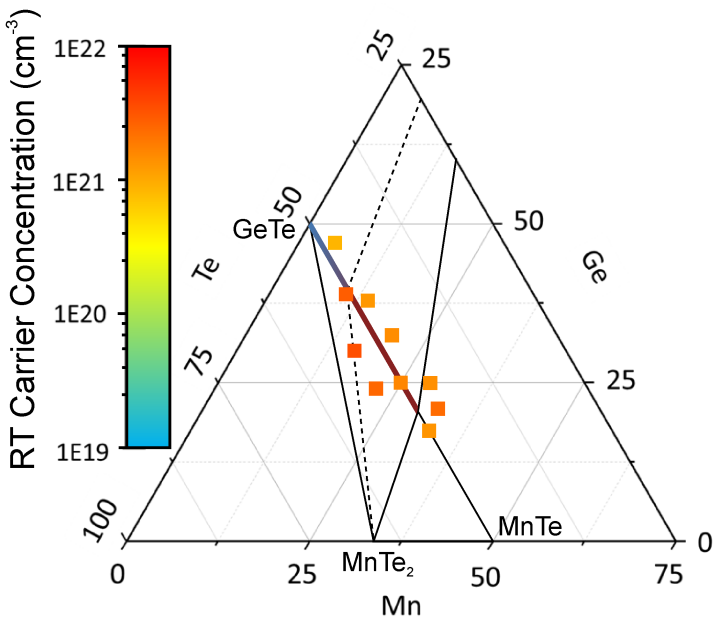

Figure 1: Carrier concentration of $Ge_{1-x}Mn_xTe$ samples and their dependence on composition. No obvious trend in carrier concentration with respect to Mn content is identified.

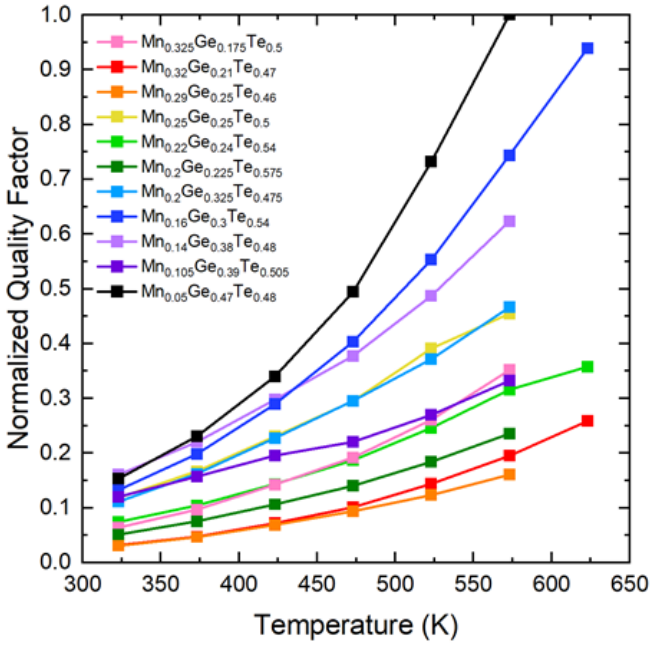

Figure 2: Quality factor shows that a moderate amount of Mn is good.

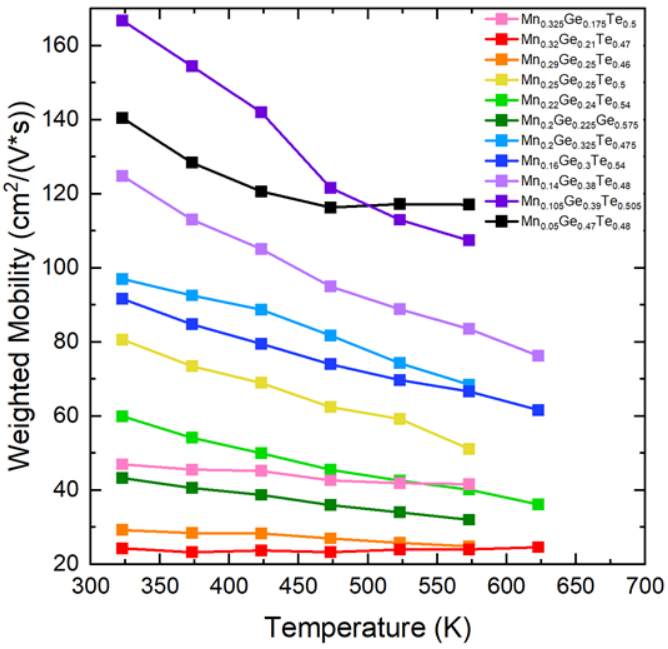

Figure 3: Weighted mobility showing an inverse dependence with temperature. Samples with a high weighted mobility are relatively low in Mn concentration.

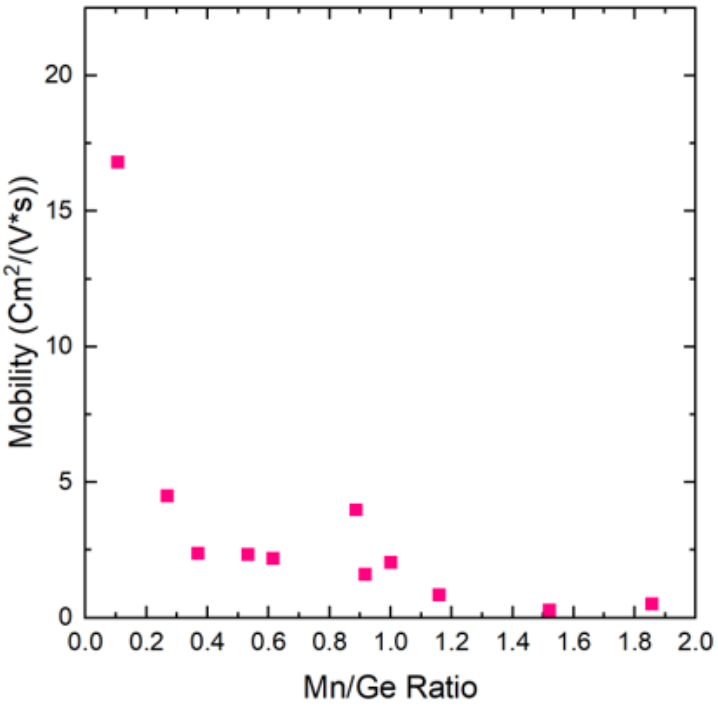

Figure 4: Hole mobility of the $Ge_{1-x}Mn_xTe$ alloy system showing an overall decrease in mobility with respect to increasing Mn content. The low mobility is likely a result of the flattening of the electronic band structure near the band edge.

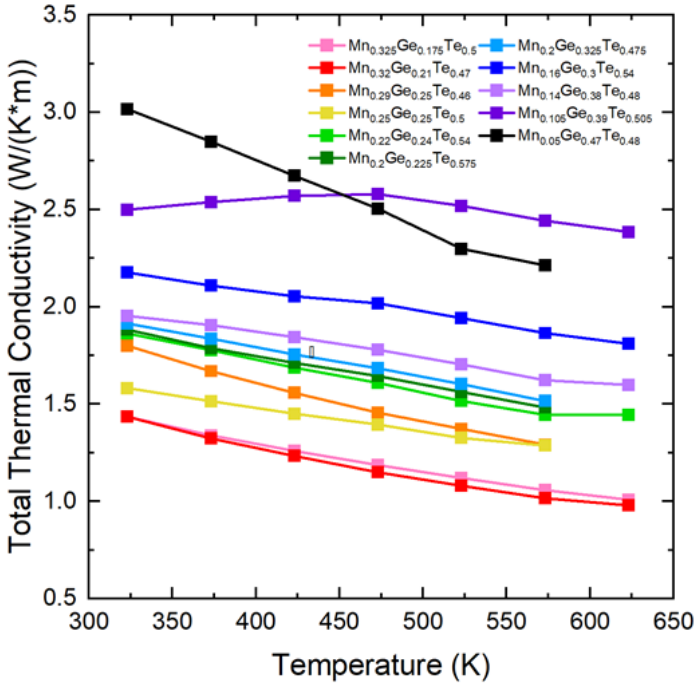

Figure 5: Total thermal conductivity becomes reduced at high temperature for most samples. In $Mn_{0.105}Ge_{0.39}Te_{0.505}$ the increase in electronic thermal conductivity is high enough to offset the decrease in lattice thermal conductivity such that the thermal conductivity is relatively flat.

Table 2: Table of experimental data

Sample	Avg. Grain Size (μm)	Density (g/cm^3)	% Ternary	% Ge	% MnTe	% $MnTe_2$
$Mn_{0.325}Ge_{0.175}Te_{0.5}$	9	5.96	100	0.0	0.0	0.0
$Mn_{0.32}Ge_{0.21}Te_{0.47}$	8	5.88	85.6	7.8	6.6	0.0
$Mn_{0.29}Ge_{0.25}Te_{0.46}$	5	5.98	90.0	6.4	3.6	0.0
$Mn_{0.25}Ge_{0.25}Te_{0.50}$	6	6.00	93.3	0.0	0.0	6.7
$Mn_{0.22}Ge_{0.24}Te_{0.54}$	14	6.05	83.9	0.0	0.0	16.1
$Mn_{0.2}Ge_{0.225}Te_{0.575}$	12	6.00	60.5	0.0	0.0	39.5
$Mn_{0.2}Ge_{0.325}Te_{0.475}$	9	6.01	97.7	2.3	0.0	0.0
$Mn_{0.16}Ge_{0.3}Te_{0.54}$	15	5.98	64.6	0.0	0.0	35.4
$Mn_{0.14}Ge_{0.38}Te_{0.48}$	11	5.95	92.4	7.6	0.0	0.0
$Mn_{0.105}Ge_{0.39}Te_{0.505}$	6	6.05	100	0.0	0.0	0.0
$Mn_{0.05}Ge_{0.47}Te_{0.48}$	8	6.01	95.4	4.6	0.0	0.0
$Mn_{0.055}Ge_{0.44}Te_{0.505}$	7	6.11	100*	0.0	0.0	0.0
$Mn_{1.1}GeTe_2$	7	5.88	94.7	5.3	0.0	0.0
$Mn_{0.29}Ge_{0.19}Te_{0.52}$	11	5.90	67.5	0.0	0.0	32.5
$MnGe_{1.1}Te_2$	7	5.90	100	0.0	0.0	0.0
$Mn_{0.4}Ge_{0.05}Te_{0.55}$	13	5.89	26.8	0.0	9.8	63.4
$MnGeTe_{2.1}$	14	5.80	92.0	0.0	0.0	8
$Mn_{0.34}Ge_{0.14}Te_{0.52}$	18	5.65	74.5	0.0	0.0	25.5
$Mn_{0.05}Ge_{0.6}Te_{0.35}$	9	5.77	70.6	0.0	29.4	0.0
$Mn_{0.25}Ge_{0.4}Te_{0.35}$	5	5.43	65.8	31.0	3.2	0.0
$Mn_{0.065}Ge_{0.41}Te_{0.525}$	7	6.06	84.7	15.3	0.0	0.0

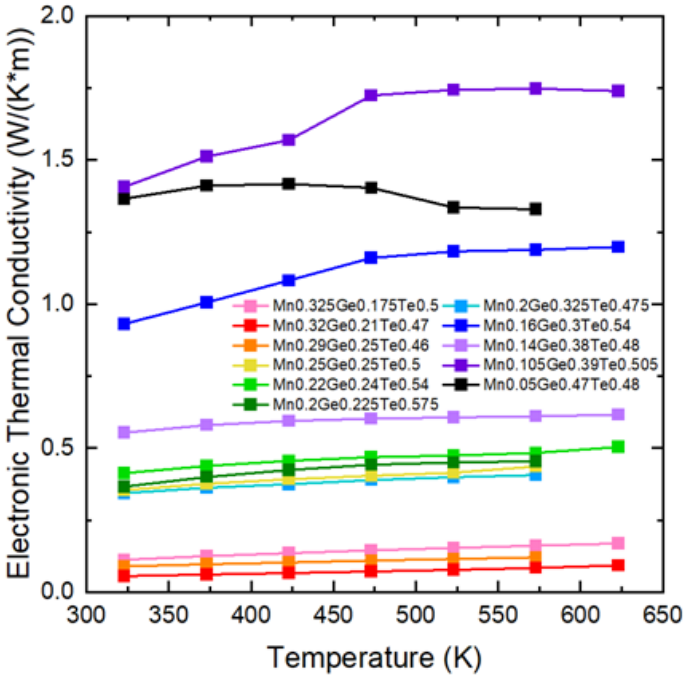

Figure 6: Electronic thermal conductivity of $Ge_{1-x}Mn_xTe$ samples increases for most samples, likely as a result of carrier activation at higher temperatures.

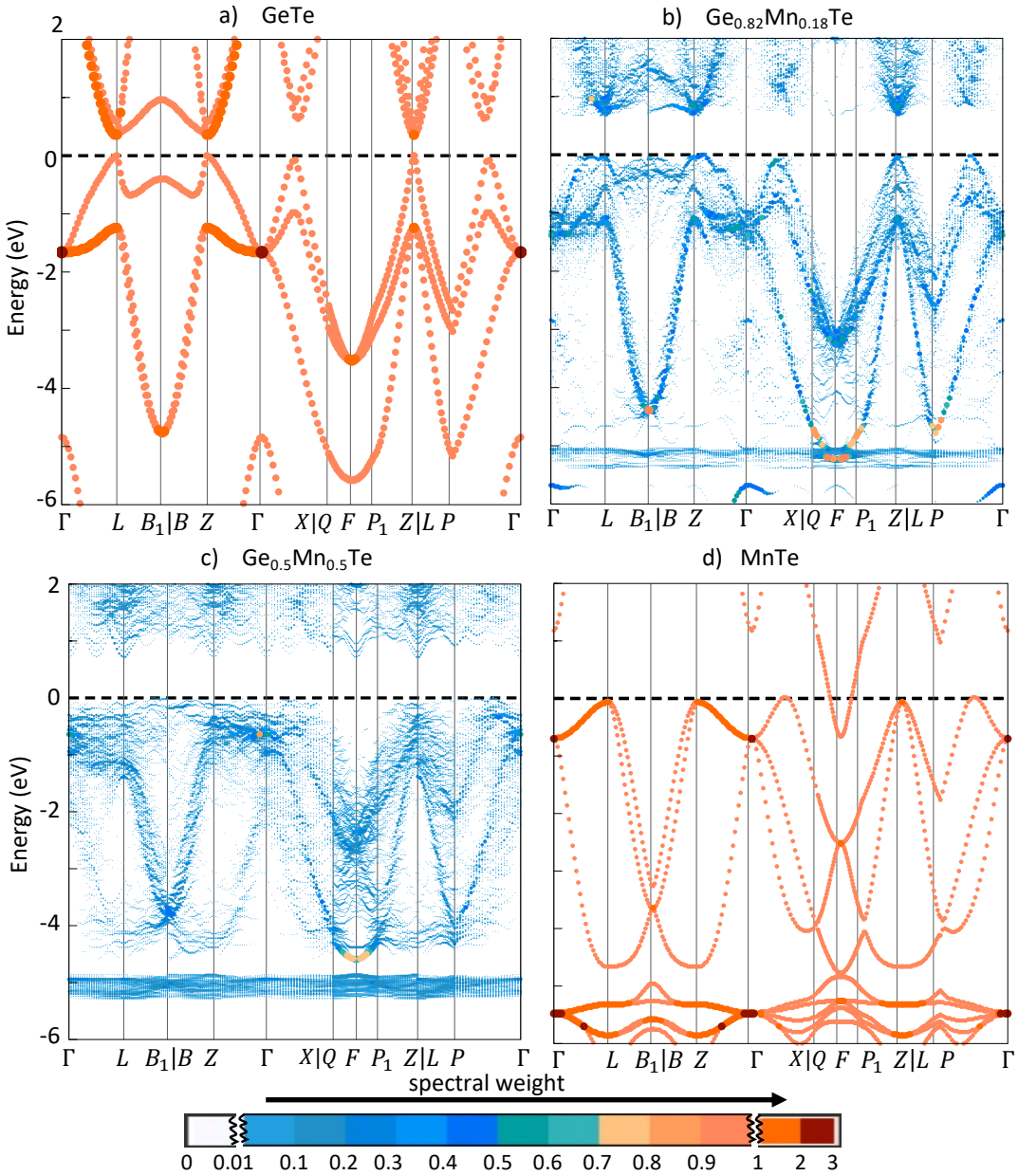

Figure 7: Band structure evolution of SQS alloy structures of rock salt $Ge_{1-x}Mn_xTe$ with $x = 0, 18.75, 50\%$ and pure MnTe. Here the evolution of band structures from GeTe $\rightarrow$ $Ge_{0.82}Mn_{0.18}Te$ $\rightarrow$ $Ge_{0.50}Mn_{0.50}Te$ $\rightarrow$ MnTe are shown in (a), (b), (c) and (d) respectively. The figures demonstrate a comparison of electronic structures of pure GeTe to SQS alloy structures and pure MnTe. For ease of comparison, the Brillouin zone path plotted for high symmetry rock salt corresponds to the same path shown for the lower symmetry rhombohedral phase.

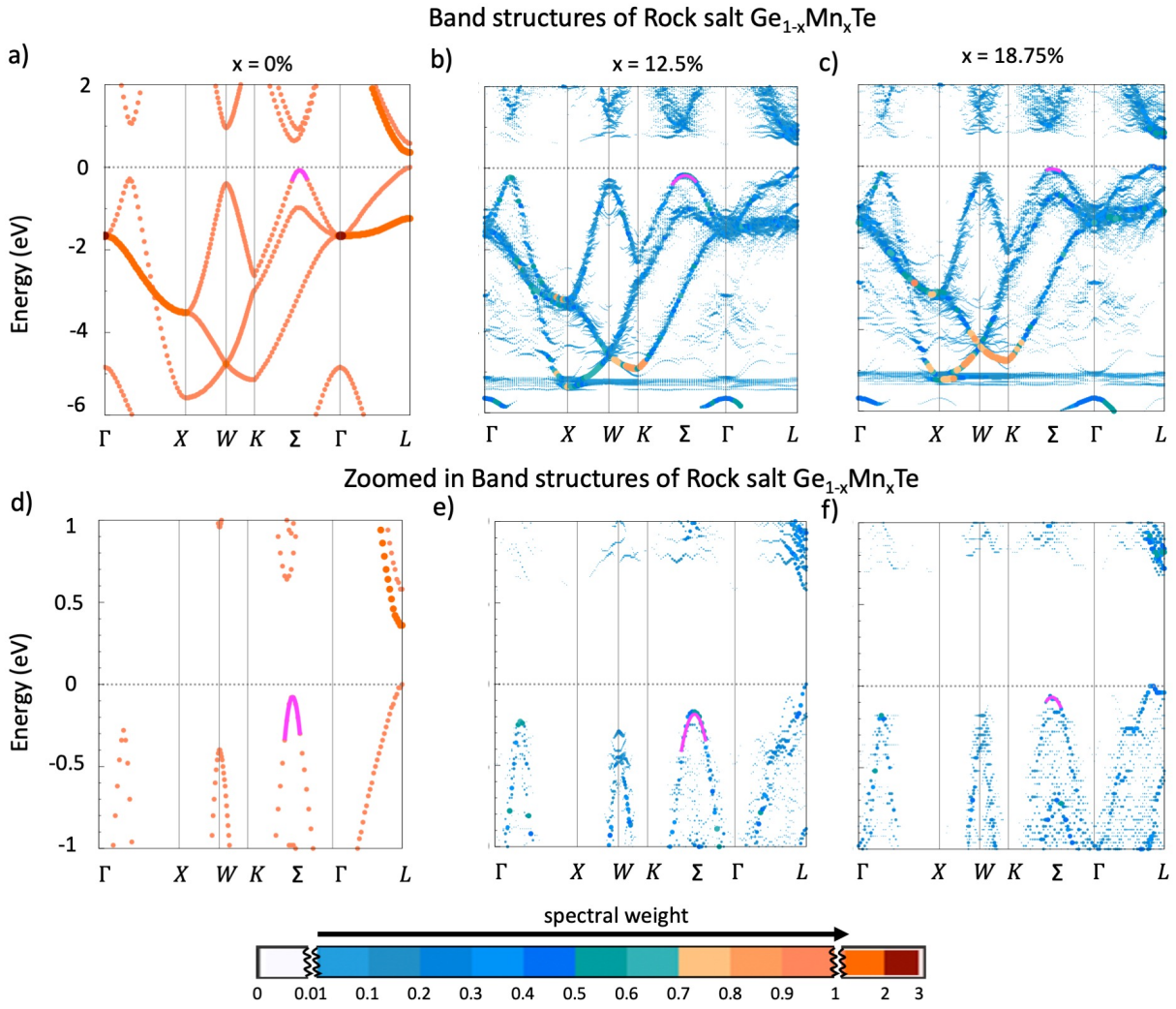

Figure 8: Band structure evolution of SQS alloy structures of rock salt $Ge_{1-x}Mn_xTe$ with $x = 0, 12.5$ and 18.75%. Here, the Brillouin zone path plotted corresponds to actual rock salt k-path of rock salt phase. The band structure evolution is shown in colorscale and fitted curvature is shown in purple color line.The top panel containing (a), (b) and (c) shows the band structure from GeTe $\rightarrow$ $Ge_{0.875}Mn_{0.125}Te$ $\rightarrow$ $Ge_{0.82}Mn_{0.18}Te$ at σ respectively. The bottom panel figures (d), (e) and (f) shows the band structure and the fitted curve in a zoomed in energy range near VBM for the same compositions. The figures demonstrate a comparison of change in curvature of pure GeTe to SQS alloy structures. The coefficient of the quadratic curvature changes from $24 \rightarrow 8 \rightarrow 4$ from from GeTe $\rightarrow$ $Ge_{0.875}Mn_{0.125}Te$ $\rightarrow$ $Ge_{0.82}Mn_{0.18}Te$ at Σ.

Method to fit parabola: It is more difficult to estimate effective masses from the VBM for unfolded band structures, where rather than a list of points xi,yi that are used to fit parabolas as in the case of a standard band structure, now we have a power density on a two-dimensional grid where each point in the grid xi,yj is given a weight wij which is equal to the number of bands that unfold back to grid point xi,yj. Our approach to fitting curvatures is to fit a parabola to the grid, aiming to fit the points with larger weights most accurately. That is, the error in the fitted parabola for each point xi,yj is weighted by wij. This results in biasing the fit to where the number of bands is largest. Please see the examples below, where the purple line shows the fitted parabola obtained in this manner.

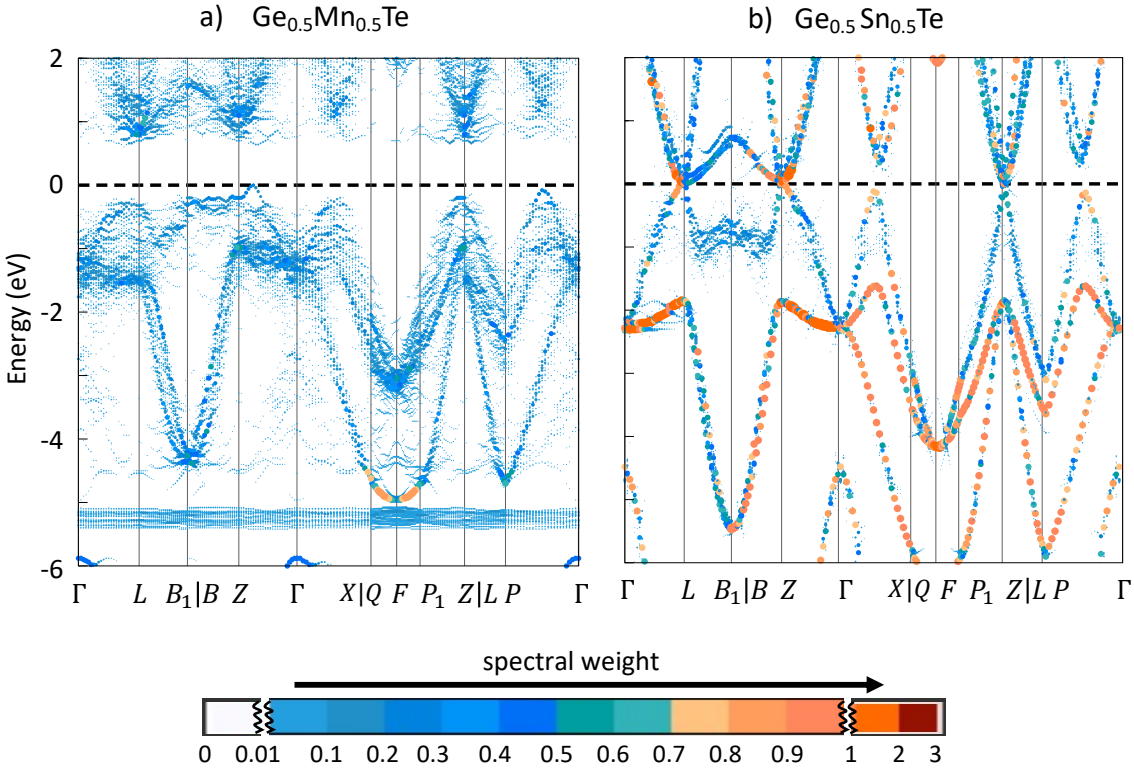

Figure 9: Band structure evolution of SQS alloy structures of rock salt a) $Ge_{0.5}$Mn0.5Te with and b) $Sn_{0.5}$Mn0.5Te. (a) The band structure shows that with high i.e 50% Mn alloying the bands are highly distorted and dispersion-less due to Mn 3d orbitals. (b) In contrast, with the same alloy percentage, i.e 50% Sn alloyed with GeTe retains well-defined and less distorted bands near VBM. The Brillouin zone path plotted for high symmetry rock salt corresponds to the same path shown for the lower symmetry rhombohedral phase.

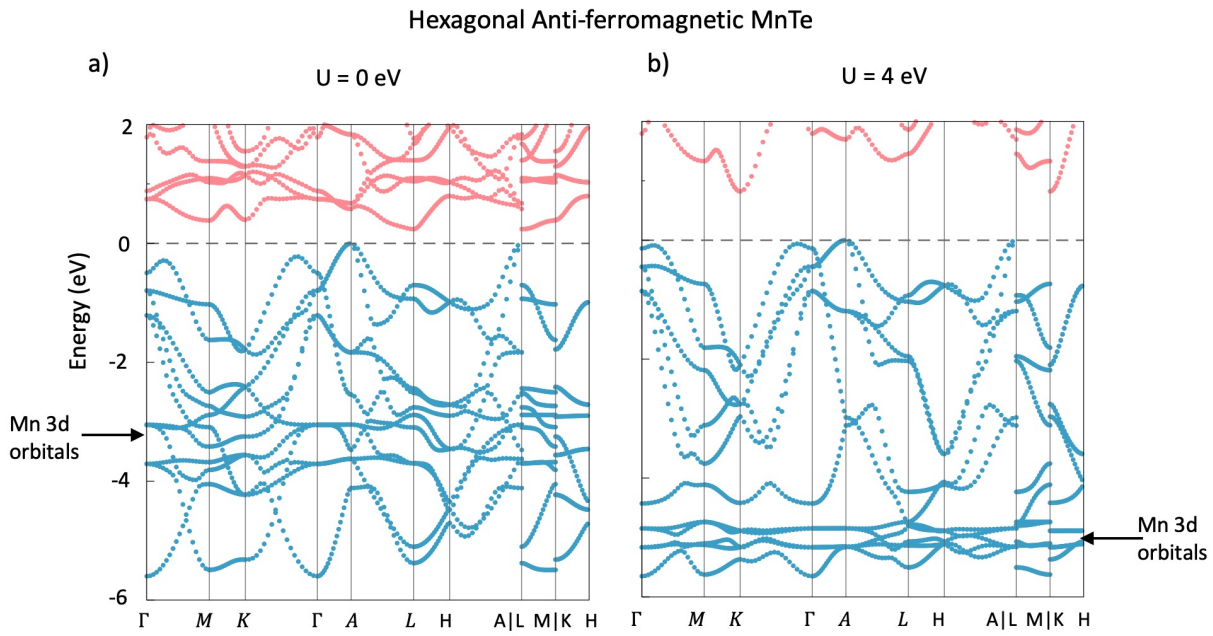

Figure 10: Band structure evolution of hexagonal MnTe with (a) U= 0 eV and (b) U = 4 eV. (a) The Mn $3d^5$ orbitals are less localized around -3 eV with a U correction is not applied with a 0.25 eV predicted band gap. (b) In contrast with U = 4 eV the Mn $3d^5$ orbitals are localized around -5 eV i.e in deeper state and more well described with respect to their 3d configuration. Here, the bandgap is 0.9 eV, closer to experimental prediction.

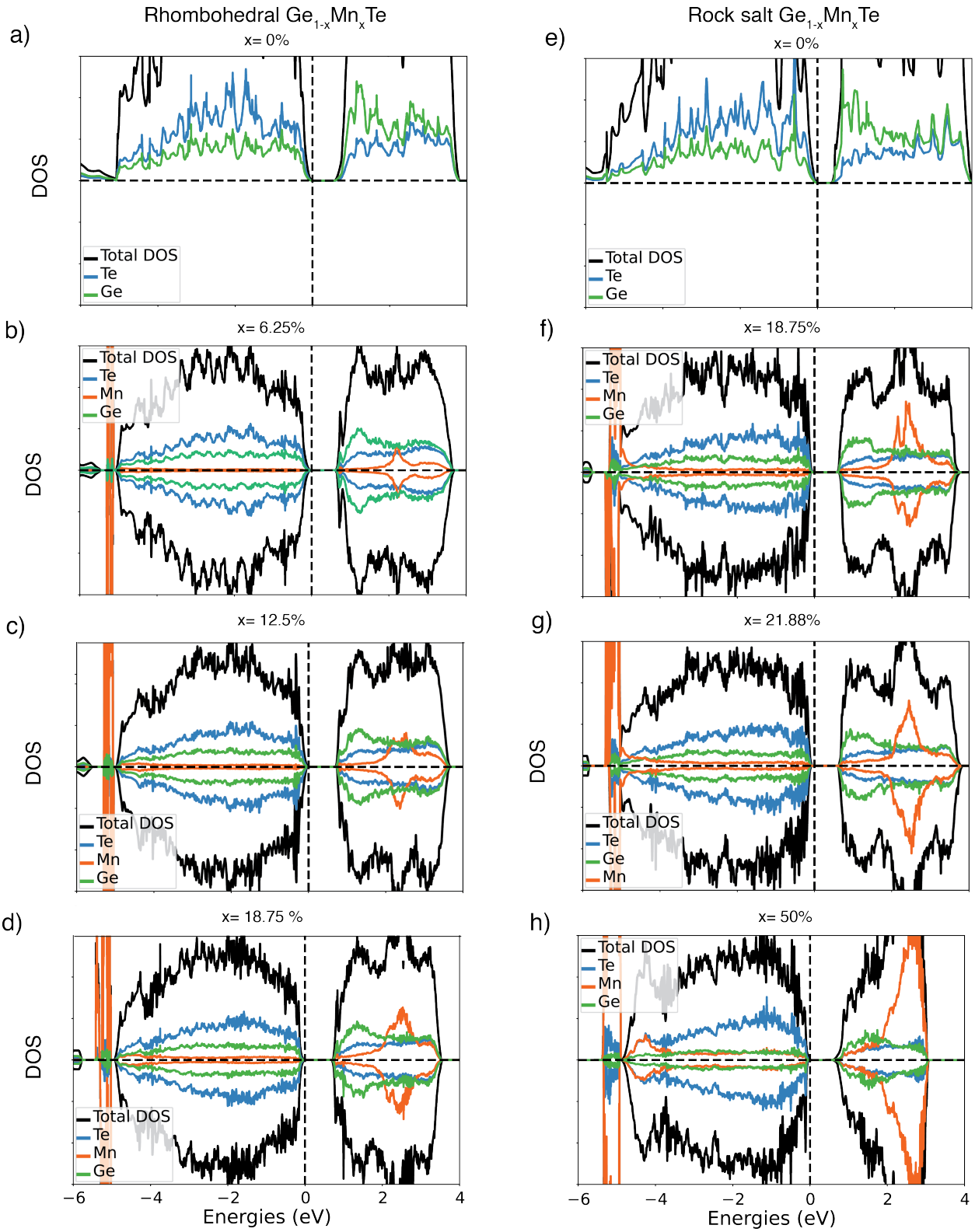

Figure 11: Density of states (DOS) for the pure GeTe phase and the alloy compositions for rhombohedral and rocksalt phase. The compositions shown here are same as the the phases that band structures were shown in main text figure 8 (a-h). To account for strong correlation of Mn atoms, U = 4 eV and a magnetism of 4.5 μ_B was considered in the alloy compositions.

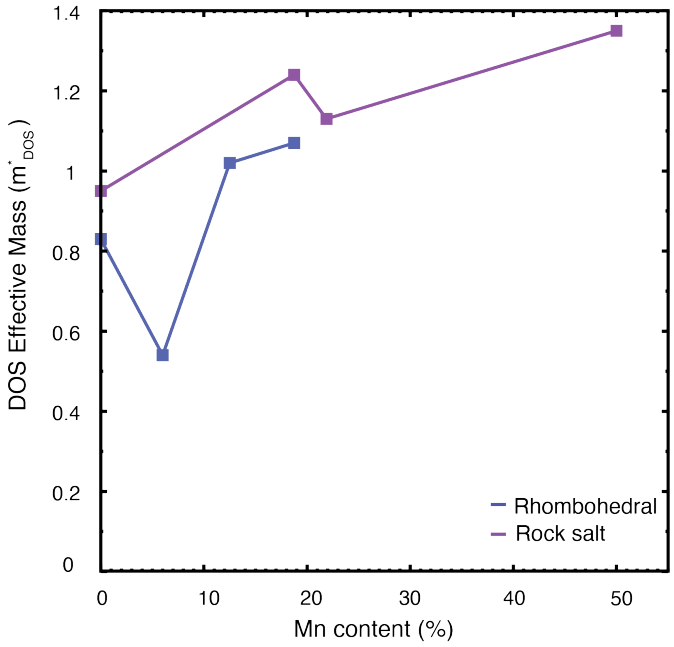

Figure 12: Comparison of DOS effective mass at VBM for Rhombohedral and Rock salt Ge_{1-x} Mn_xTe alloys. The DOS effective masses extracted from the total DOS plots above are noisy, but generally show an increasing trend with Mn incorporation. We have considered a 200 meV energy window for fitting the DOS.

$Mn_{0.325}Ge_{0.175}Te_{0.5}$

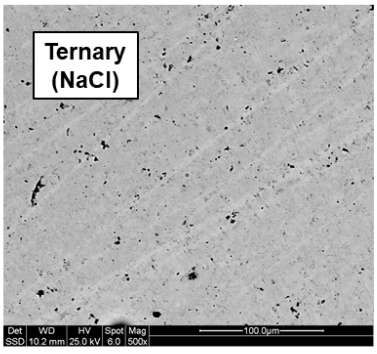

Ternary

Element	Atomic %
Te	46.84
Mn	31.65
Ge	21.51

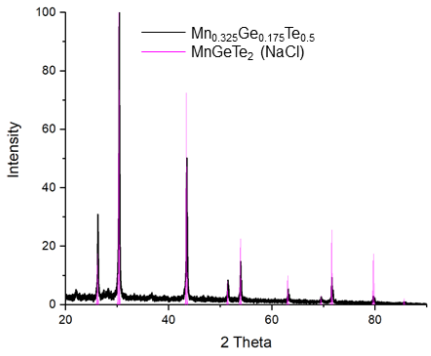

Figure 13: Used for electronic transport data in main body. Sample shows a clean microstructure and XRD pattern, indicating good behavior.

$Mn_{0.32}Ge_{0.21}Te_{0.47}$

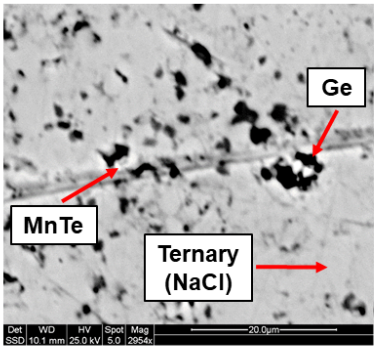

Ternary

Element	Atomic %
Te	45.77
Mn	30.21
Ge	24.01

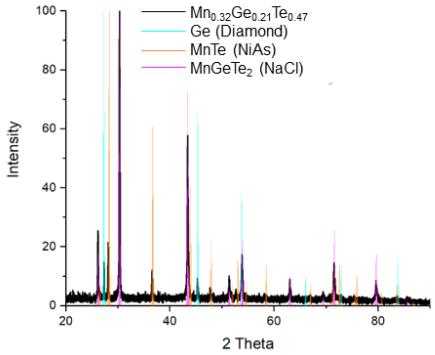

Figure 14: Used for electronic transport data in main body. Sample shows porosity and the presence of minor Ge and MnTe impurities in the SEM micrograph and XRD pattern.

$Mn_{0.29}Ge_{0.25}Te_{0.46}$

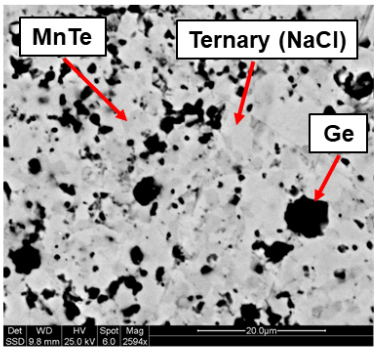

Ternary

Element	Atomic %
Te	45.12
Mn	23.78
Ge	31.10

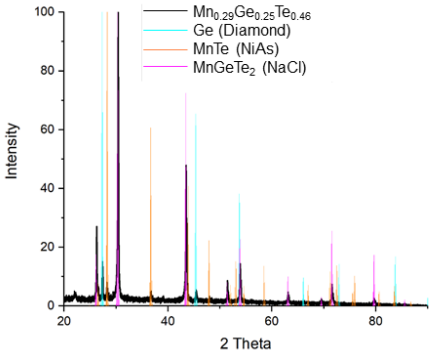

Figure 15: Used for electronic transport data in main body. Sample shows a significant MnTe and Ge impurities in both the SEM micrograph and XRD pattern.

$MnGeTe_2$

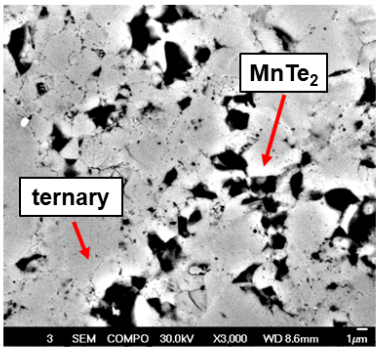

Ternary

Element	Atomic %
Te	47.45
Mn	27.53
Ge	25.01

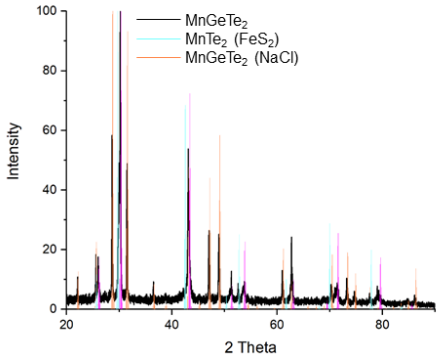

Figure 16: Used for electronic transport data in main body. Sample shows small pores and $MnTe_2$ impurity phases in the microstructure. $MnTe_2$ impurity phases are also identified in the XRD pattern.

$Mn_{0.22}Ge_{0.24}Te_{0.54}$

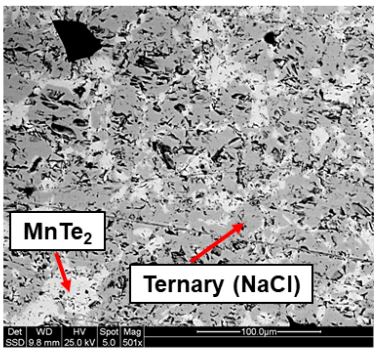

Ternary

Element	Atomic %
Te	44.79
Mn	17.52
Ge	37.7

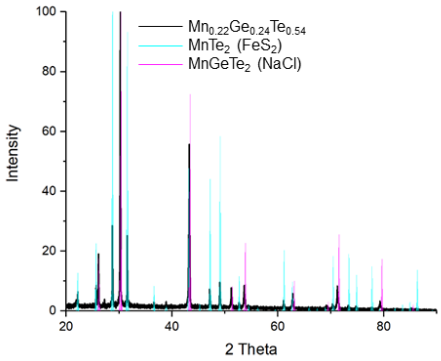

Figure 17: Used for electronic transport data in main body. Sample shows a microstructure with a significant phase fraction of $MnTe_2$ in the SEM micrograph and XRD pattern.

$Mn_{0.2}Ge_{0.225}Te_{0.575}$

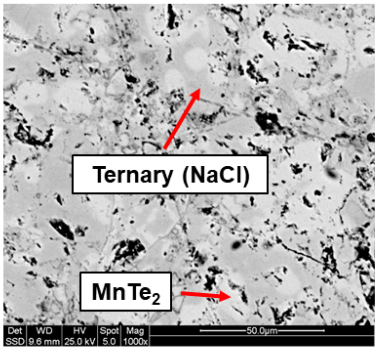

Ternary

Element	Atomic %
Te	44.3
Mn	8.34
Ge	47.37

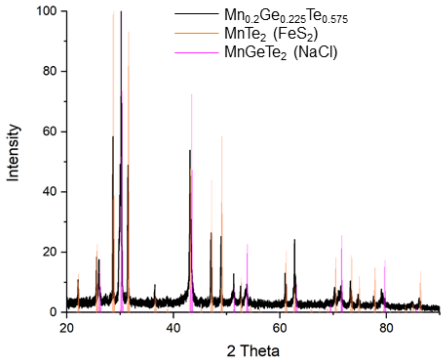

Figure 18: Used for electronic transport data in main body. Sample shows minor porosity along with a significant phase fraction of $MnTe_2$ in the SEM micrograph and XRD pattern. The low concentration of Mn in the matrix phase indicates behavior will be different from other samples rich in $MnTe_2$ but with a higher Mn content in the ternary matrix.

$Mn_{0.2}Ge_{0.325}Te_{0.475}$

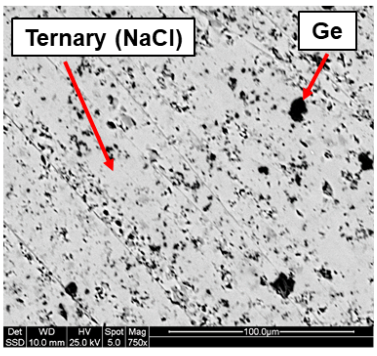

Ternary

Element	Atomic %
Te	45
Mn	19.61
Ge	35.4

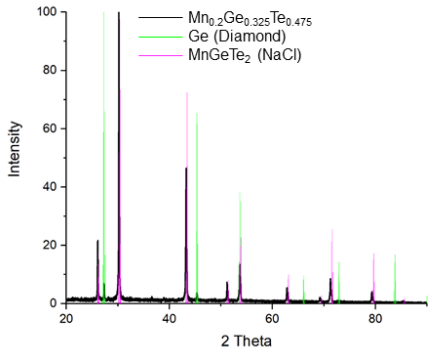

Figure 19: Used for electronic transport data in main body. Sample shows minor porosity and a small fraction of Ge inclusions as evident by the SEM micrgraph and XRD pattern.

$Mn_{0.16}Ge_{0.3}Te_{0.54}$

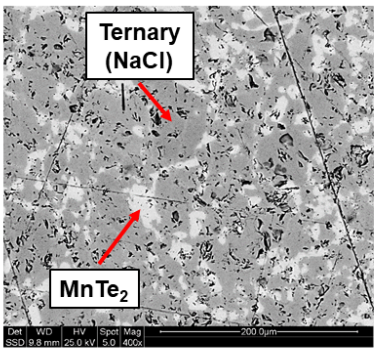

Ternary

Element	Atomic %
Te	44.14
Mn	11.8
Ge	44.06

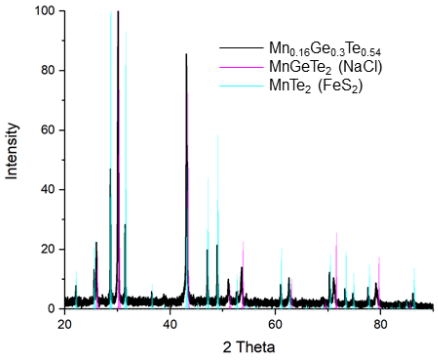

Figure 20: Used for electronic transport data in main body. Sample shows a significant phase fraction of $MnTe_2$ in both the SEM micrograph and XRD pattern.

$Mn_{0.14}Ge_{0.38}Te_{0.48}$

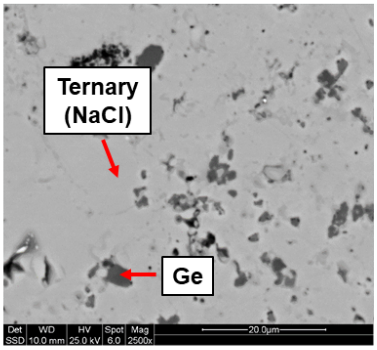

Ternary

Element	Atomic %
Te	43.8
Mn	13.61
Ge	42.58

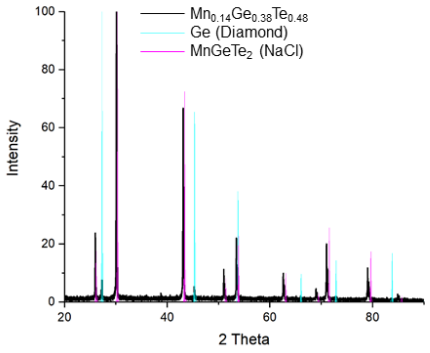

Figure 21: Used for electronic transport data in main body

$Mn_{0.105}Ge_{0.39}Te_{0.505}$

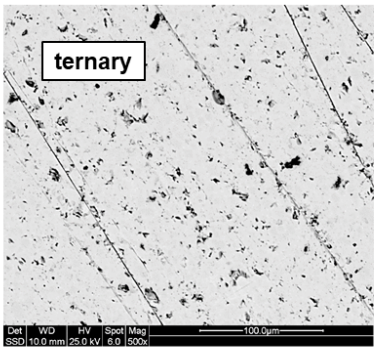

Ternary

Element	Atomic %
Te	43.97
Mn	8.8
Ge	47.23

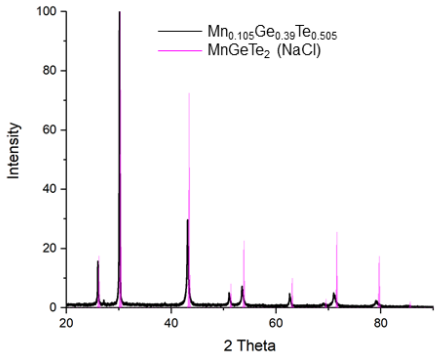

Figure 22: Used for electronic transport data in main body. Sample shows a minor fraction of Ge and negligible porosity.

$Mn_{0.05}Ge_{0.47}Te_{0.48}$

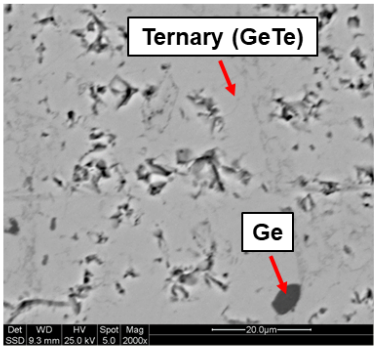

Ternary

Element	Atomic %
Te	41.08
Mn	4.37
Ge	54.55

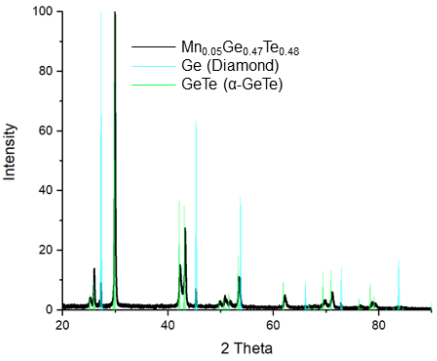

Figure 23: Used for electronic transport data in main body. Sample shows minor Ge impurities in a GeTe structured matrix. The dilute concentration of Mn is not enough to push the structure into a rock salt phase.

$Mn_{0.055}Ge_{0.44}Te_{0.505}$

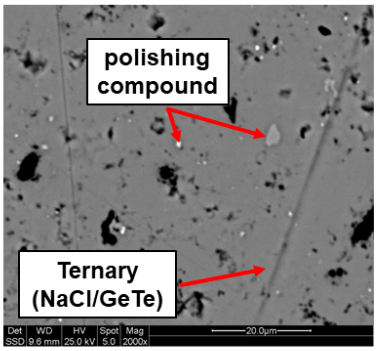

Ternary

Element	Atomic %
Te	43.15
Mn	4.4
Ge	52.46

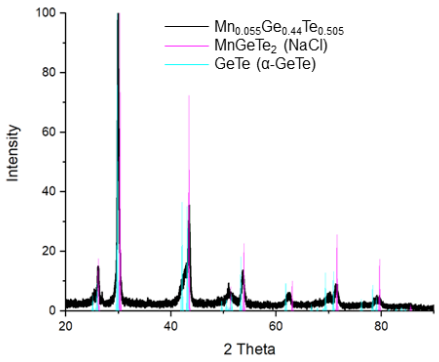

Figure 24: Electronic transport data measured but not included in main text of paper. SEM of the sample shows some minor surface artifacts from the polishing process. The XRD pattern of the sample suggests that the sample is metastable near the transition from rhombohedral GeTe to rock salt structure.

$Mn_{1.1}GeTe_2$

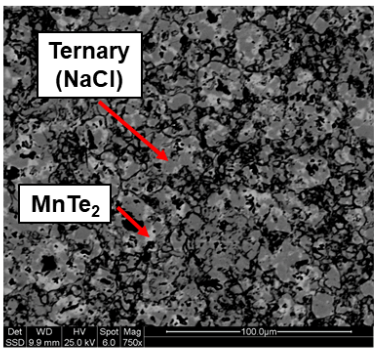

Ternary

Element	Atomic %
Te	44.94
Mn	20.44
Ge	34.63

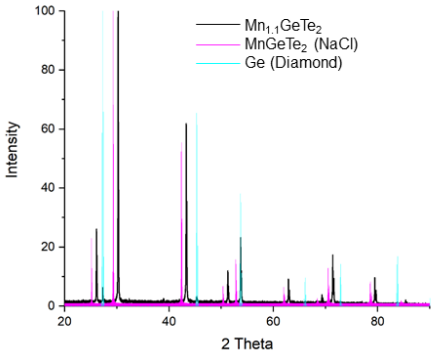

Figure 25: Electronic transport data measured but not included in main text of paper. Sample shows significant fractions of $MnTe_2$ and Ge in the SEM micrograph. Only the ternary phase and Ge are identified in the XRD pattern.

$Mn_{0.29}Ge_{0.19}Te_{0.52}$

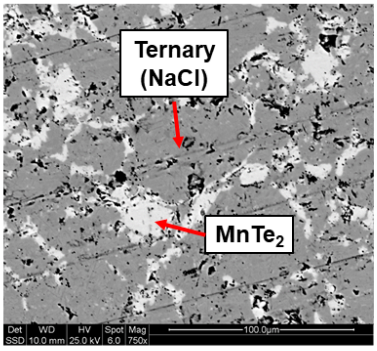

Ternary

Element	Atomic %
Te	46.4
Mn	26.32
Ge	27.28

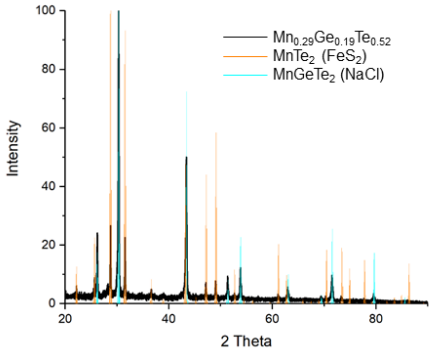

Figure 26: Electronic transport data measured but not included in main text of paper. Sample shows significant fractions of $MnTe_2$ in the SEM micrograph and XRD pattern.

$MnGe_{1.1}Te_2$

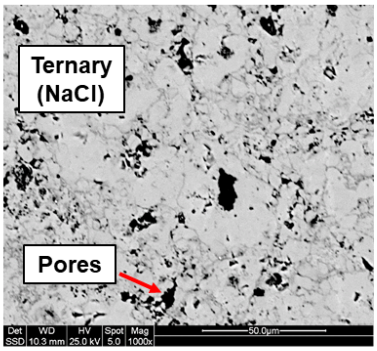

Ternary

Element	Atomic %
Te	45.54
Mn	22.37
Ge	32.1

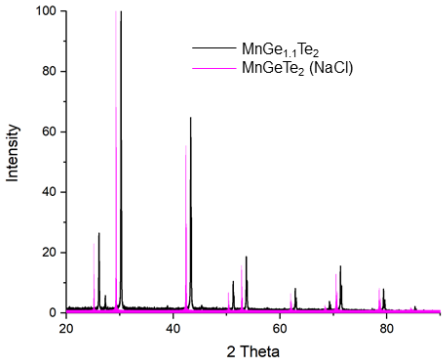

Figure 27: Electronic transport data measured but not included in main text of paper. Sample shows only 1 phase in the SEM micrograph along with minor porosity. The left-shifted peaks in the XRD pattern indicate a higher GeTe concentration in the rock salt structure.

$Mn_{0.4}Ge_{0.05}Te_{0.55}$

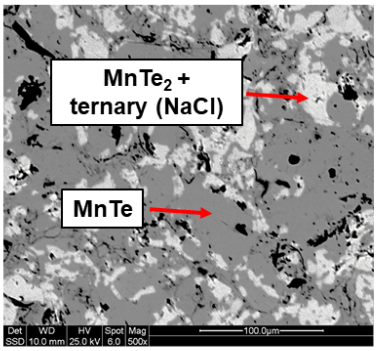

$MnTe_2$

Element	Atomic %
Te	65.87
Mn	33.98
Ge	0

MnTe

Element	Atomic %
Te	49.09
Mn	48.31
Ge	2.6

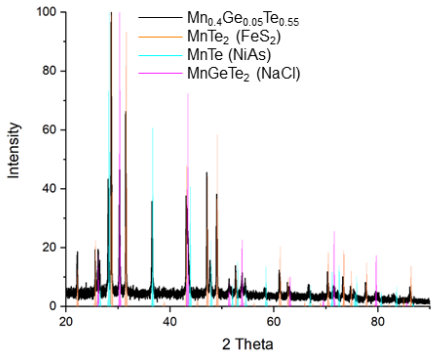

Figure 28: Electronic transport data measured but not included in main text of paper. Sample shows nonequilibrium behavior as $MnTe_2$ and the ternary have a microstructure that resembles rapid solidification.

$MnGeTe_{2.1}$

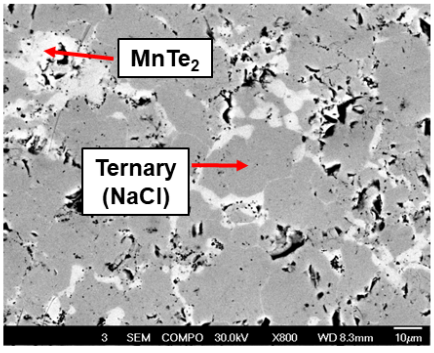

Ternary

Element	Atomic %
Mn	24.27
Ge	26.24
Te	49.47

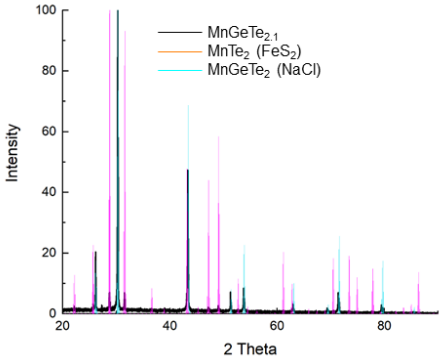

Figure 29: Electronic transport data measured but not included in main text of paper. Sample hows significant $MnTe_2$ concentration in the rock salt matrix.

$Mn_{0.34}Ge_{0.14}Te_{0.52}$

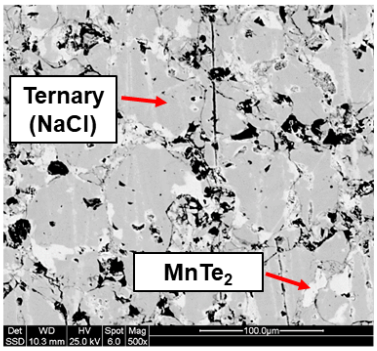

Ternary

Element	Atomic %
Te	47.04
Mn	31.75
Ge	21.22

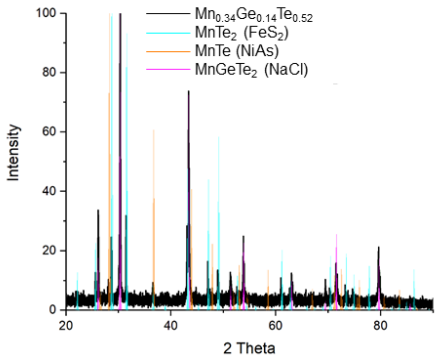

Figure 30: Electronic transport data measured but not included in main text of paper. Sample shows significant $MnTe_2$ concentration in the SEM micrograph. MnTe is present in the XRD pattern, however, no MnTe was found by SEM.

$Mn_{0.05}Ge_{0.6}Te_{0.35}$

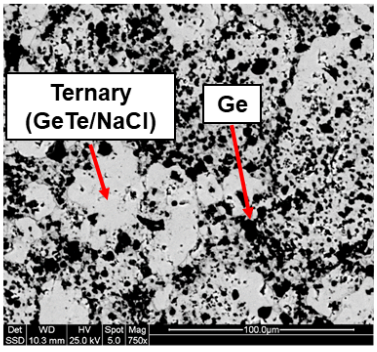

Ternary

Element	Atomic %
Te	42.45
Mn	3.65
Ge	53.92

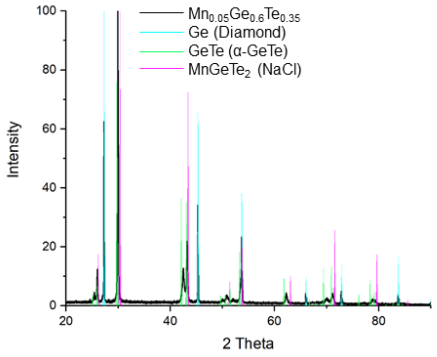

Figure 31: Electronic transport data measured but not included in main text of paper. Sample shows a significant fraction of Ge impurity phase in the GeTe/NaCl ternary. The XRD pattern shows both the rock salt and GeTe structures to highlight the similarity between the two patterns. The α-GeTe structure was used for Rietveld refinement.

$Mn_{0.25}Ge_{0.4}Te_{0.35}$

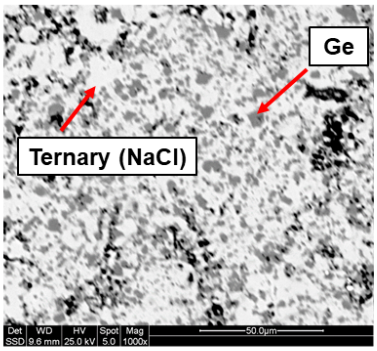

Ternary

Element	Atomic %
Te	44.23
Mn	28.57
Ge	27.2

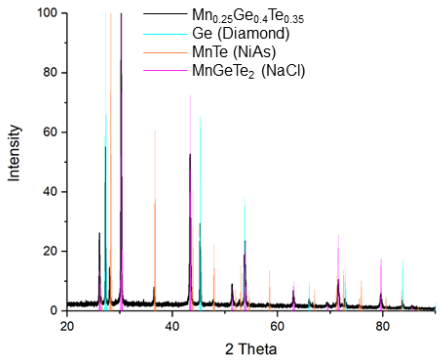

Figure 32: Electronic transport data measured but not included in main text of paper. Sample shows a significant concentration of Ge impurity phase in the SEM micrograph. MnTe is present in the XRD pattern but was not identified by SEM.

$Mn_{0.065}Ge_{0.41}Te_{0.525}$

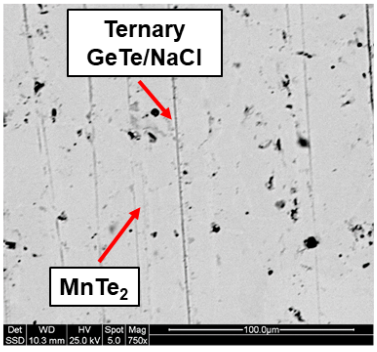

Ternary

Element	Atomic %
Te	44.66
Mn	4.19
Ge	51.15

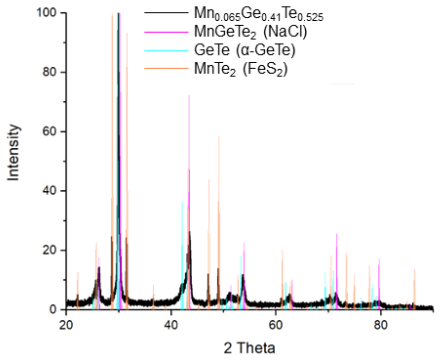

Figure 33: Electronic transport data measured but not included in main text of paper. Sample shows a relatively clean microstructure with minor $MnTe_2$ impurity phases. The XRD pattern suggests the sample may not be at equilibrium and could be transitioning from rock salt to rhombohedral.

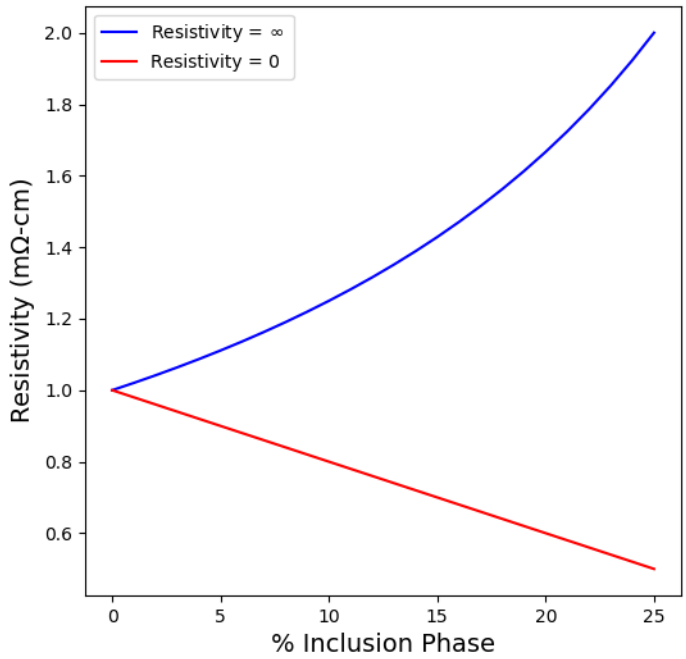

Figure 34: Plot of effective media showing how an infinitely resistive inclusion phase (i.e. pores) will affect the resistivity of a sample.